RSC Advances

PAPER

View Article Online
View Journal | View Issue

Cite this: *RSC Adv.*, 2024, **14**, 37993

Drug molecules beyond chemical biology: fluorescence- and DFT-based investigations for fluoride ion sensing and the trace detection of chloroform†

Sohail Anjum Shahzad, *[a] Tayyeba Javid,[a] Mohammed A. Assiri,[bc] Aqsa Pervaiz,[a] Hasher Irshad,[a] Fu-She Han [d] and Di Demi He[e]

Excessive unmonitored use of fluoride has remained a threatening issue for a long time now as its long-term use is linked to several health issues. Similarly, chloroform is a highly carcinogenic solvent that requires proper monitoring. The increasing demand for a convenient, selective and sensitive fluoride and chloroform sensor intrigued us to utilize etoricoxib (**ECX**) as a sensor as it is highly safe and easily available. The photophysical properties of **ECX**, which were previously unexplored, were now studied with increasing water fractions and a significant aggregation-induced emission enhancement (AIEE) was seen through fluorescence spectroscopy. **ECX** was also successfully used for the trace level detection of chloroform through a significant emission enhancement. Similarly, the **ECX**-based sensor successfully detected fluoride ions by showing enhancement in emission intensity with maximum emission wavelength at 373 nm. Through fluorescence titration experiments, the effects of different conditions and interfering species on the sensing efficiency of **ECX** were studied, and the results showed that the sensor was highly selective and sensitive towards fluoride, with a limit of detection of 20 nM. Other than fluorescence spectroscopy, the type of interaction between the sensor and analyte was also studied through UV-Vis spectroscopy, revealing a non-covalent type of interaction, which was further validated through DFT studies. Frontier molecular orbital (FMO) analysis was performed along with density of state (DOS) studies to investigate the energy levels of the orbitals. Non-covalent interaction (NCI) and natural bond orbital (NBO) analysis provided information about the types of interaction and charge transfer. **ECX** has the potential to be used for real-time sensing applications and could be used for sensing moisture and fluoride in real samples.

Received 4th July 2024
Accepted 6th November 2024

DOI: 10.1039/d4ra04844j

rsc.li/rsc-advances

Introduction

Fluorescent sensors that can specifically target an analyte has become a necessity for sustaining a healthy and safe environment for the sake of all life forms. Many researchers are working on monitoring the increasing concentration of unwanted hazardous substances through fluorescent sensors in various biological and environmental fields.[1] High affinity towards a particular analyte and production of a detectable response upon binding to the analyte without any influence from environmental interferences are the basic requirements of an ideal fluorescent sensor.[2] Development of the first fluorescent chemosensor for aluminum ion detection (Al^{3+}) in 1867 by Friedrich Goppelsröder provided the motivation for designing and utilizing fluorescent sensors for various ionic species.[3–5] Anions have widespread use in biological, pharmaceutical, environmental, and chemical processes. The smallest anion fluoride (F^-), bearing a high charge density, has been the center of attention for several researchers.[6] Fluoride is used worldwide for dental care and osteoporosis treatment.[7] Fluoride also finds applications in the military for weapon manufacturing and nerve gas monitoring.[8] Due to the excessive demand for fluoride for healthy bones, teeth, nails and hair, it can be found in drinking water, toothpaste, gels, mouthwash, food products and pharmaceuticals.[9] Once fluoride enters the body through different sources, it gets absorbed in the bones and cannot be

[a]*Department of Chemistry, COMSATS University Islamabad, Abbottabad Campus, University Road, Abbottabad 22060, Pakistan. E-mail: sashahzad@cuiatd.edu.pk*
[b]*Department of Chemistry, Faculty of Science, King Khalid University, P. O. Box 9004, Abha 61413, Saudi Arabia*
[c]*Central Labs, King Khalid University, AlQura'a, Abha, P. O. Box 960, 61413, Saudi Arabia*
[d]*Changchun Institute of Applied Chemistry, Chinese Academy of Science, 5625 Renming Street Changchun, Jilin 200032, China*
[e]*State Key Laboratory of Electroanalytical Chemistry, Changchun Institute of Applied Chemistry, Chinese Academy of Sciences, Changchun, 130022, P. R. China*

† Electronic supplementary information (ESI) available. See DOI: https://doi.org/10.1039/d4ra04844j

removed easily, potentially leading to skeletal and dental fluorosis. Dental fluorosis is the discoloration of teeth enamel, which can permanently darken in severe cases, and its leading cause is the excessive consumption of fluoride at a young age. Skeletal fluorosis is accompanied by stiffness and pain in the joints, which can lead to paralysis or disability.[10] Fluoride was observed to be a neurotoxicity-causing factor in animals and humans.[11] The intake of fluoride was also reported to be harmful during pregnancy as fluoride is capable of crossing the placenta, which means it can affect the blood concentration of the fetus.[12] Moreover, excess amounts of fluoride can cause kidney diseases, gastric disorders, cancer, and can even lead to death.[13] According to the US Environmental Protection Agency (EPA, USA) and World Health Organization (WHO), the in drinking water fluoride content should not exceed 1.5 mg L^{-1} in drinking water.[14] Despite this, fluoride consumption is alarmingly high around the globe. Therefore, its monitoring and detection are a pressing matter and prompting the demand for a suitable sensing method for the effective detection of fluoride ions.[15]

Gas chromatography-mass spectrometry (GC-MS), ion chromatography, ion selective electrodes, and colorimetry are some available techniques for fluoride ion detection.[16] However, their typically high cost, requirement for highly trained individuals for operation, complex sample preparation requirement, and time-consuming sophisticated instruments are some of the key issues associated with these techniques. Fluorescence spectroscopy has attracted increasing interest in the sensing field due to its high selectivity, easy operation, quick response time, and high sensitivity.[17] Fluorescence spectroscopy allows the detection of molecules by tracing their emitted radiation when they de-excite. The intensity of the emitted radiation changes under certain conditions depending on whether the fluorescent compound is completely soluble in solution form or is in an aggregated state.[18] When a compound with no fluorescence emission in the solution phase starts showing high emission intensity upon aggregation, it undergoes an aggregation-induced emission (AIE) phenomenon.[19] If a fluorophore is somewhat emissive in solution phase and upon aggregation its emission intensity has further increased, the phenomenon of aggregation-induced emission enhancement (AIEE) is involved.[20,21] However, in some cases, the emission intensity of fluorophores gets reduced in the aggregated state compared to its emission intensity in the solution phase, and this type of change in emission intensity is linked to aggregation-caused quenching (ACQ).[22] As ACQ leads to a reduction in fluorescence emission because of π–π stacking, ACQ is usually an undesirable attribute in fluorescent compounds, leading to limited applications of such fluorescent compounds.[23] On the flip side, compounds exhibiting the AIEE phenomenon find application in several fields. Various factors, such as restricted intramolecular rotations (RIRs), vibrations (RIV), and motions (RIM), are responsible for inducing AIEE properties in compounds.[24,25] Therefore, AIEE is a highly favored phenomenon that can be seen in fluorescent compounds. Other than showing the AIEE and ACQ phenomena, some compounds have a tendency to show changes in the fluorescence emission intensity, color, or maximum emission wavelength (λ_{max}) when added to different solvents of varying polarity. This process is termed solvatochromism.[26] Solvatochromism is linked to electronic transitions, mainly n–π* and π–π*, that take place during the excitation of molecules.[27] The addition of a polar solvent can lead to an increase in λ_{max} causing a bathochromic shift, while non-polar solvents cause a hypsochromic shift for most compounds. Polar solvents stabilize antibonding orbitals and the energy gap of electronic levels get reduced, resulting in an emission of photons of less energy and longer wavelength, hence showing a red-shift.[28,29]

Fluorophores with such remarkable photophysical properties have high potential for use as sensors with several potential applications in different fields. Various examples of highly selective and sensitive fluorescent sensors are available in the literature, such as an AIEE-active sensor for drotaverine,[30] stilbene-based fluorescent detector for mefenamic acid,[31] substituted triazine probe for hydrogen peroxide detection,[32] triphenylamine-based sensor for 4-nitrophenol,[33] triazene-based detector for Hg^{2+},[34] probe for zinc,[35] 8-aminoquinoline-derived sensor,[36] and some nitrobenzene sensors, including a naphthalamide-based probe,[37] isophthalamide-based sensor,[38] stilbene-based sensor,[39] deferasirox-based sensor,[40] and probe for esomeprazole.[41] Etoricoxib, having anti-inflammatory properties, is a drug for the treatment of osteoarthritis, migraine, gouty arthritis, back pain and cancer prevention.[42] With a molecular weight of 358.842 g mol^{-1}, it is commonly found as a white or off-white powder and has a melting point of 126 °C. Etoricoxib containing aromatic rings and heteroatoms can exhibit significant photophysical properties; however, unfortunately these properties of etoricoxib have remained highly underexplored. Moreover, the presence of π-conjugation and heteroatoms, such as S, O, and N, in etoricoxib's structure intrigued us to investigate it as a sensor for the detection of certain analytes.

As a continuation of our research group's work for bringing such sensors to light that have the potential for detecting certain analytes, we selected etoricoxib to investigate it as a potential sensor.[43–48] Etoricoxib's (**ECX**) potential as an effective sensing for fluoride ions and chloroform was thus investigated under different conditions. Etoricoxib (**ECX**) demonstrated a prominent enhancement in fluorescence emission in the presence of fluoride ions, with similar results demonstrated with real samples, indicating the potential of this sensor for practical application. Evidence for the detection of fluoride was provided through DFT studies. Moreover, having AIEE properties, **ECX** could efficiently detect the moisture content in real samples. To the best of our knowledge, **ECX** is the first reported drug that has been used as a fluorescent sensor for F^- detection. **ECX** is not toxic and is an FDA-approved drug that is a selective inhibitor of cyclooxygenase-2 (COX-2), an enzyme involved in pain and inflammation. **ECX** was found to be highly selective and sensitive toward F^- ions, even at a very low concentration of fluoride. Due to its unique photophysical properties, **ECX** was able to efficiently detect F^- in real water samples.

Experimental

Chemicals and materials

Details about all the chemicals and instruments used for all the experiments are provided in the ESI.†

Real sample preparation

Two toothpastes, Sensodyne (A) and Colgate Max Fresh (B), from different companies were purchased from the market and 1000 mg of each toothpaste was extracted with water. Each obtained extract was sonicated and filtered to get a clear solution in 100 mL of water. Next, 10–50 μL of the toothpaste extracts A and B was spiked into 50 μM **ECX** sensor solution in DMF : water (1 : 4). The emission intensity of the **ECX** sensor was examined to illustrate the concentration of fluoride in the spiked samples A and B.

Fluorescence experiments

To study the emissive behavior of the sensor etoricoxib (**ECX**), its 50 μM concentration was optimized in DMF : water (1 : 4, v/v) solution. This optimized concentration 50 μM was further utilized for titration experiments. Moreover, 1000 μM stock solution of different anions, including F^-, CH_3COO^-, HSO_4^-, CN^-, Cl^-, SO_4^{2-}, Br^-, I^-, ClO^-, and NO_3^-, were prepared. The emission behavior of the **ECX** sensor was analyzed by gradually varying the concentration of all these anions from 0 to 50 μM and obtaining their emission spectra. The emission studies of the **ECX** sensor were carried out at an excitation wavelength (λ_{exc}) of 285 nm.

Computational studies

To perform the theoretical studies, Gaussian 09 software was used. Gauss view 5.0 was used to assess and visualize the output data simulated on Gaussian 09.[49] Furthermore, GaussSum,[50] Multiwfn 3.7,[51] and VMD[52] were also used for visualization purposes. The functional B3LYP was used for geometry optimization of the **ECX** sensor[53] and ωB97XD was used to calculate the interaction energy between the **ECX** sensor and F^-.[54] Both the geometry optimization and interaction energy calculations were performed using a 6-31G(d,p) basis set. B3LYP and ωB97XD are widely accepted functionals that can be used to elucidate the structural properties and non-covalent interactions between interacting molecules. To determine the best interaction site between the interacting molecules, the interaction energies were calculated at various possible sites of interaction. The basis set super position error (BSSE) was employed to determine the interaction energy at different possible interaction sites using the following equation:

$$E_{int} = E_c - (E_a + E_s) + E_{BSSE}$$

where E_c represents the energy of the complex **ECX**-F^-, E_a is the energy of the analyte (F^-), E_s corresponds to the energy of the sensor, and BSSE corresponds to the basis set super position error. Moreover, to elucidate the electronic properties of interacting moieties, various types of analyses, including natural bond orbital (NBO), density of states (DOS), and frontier molecular orbital (FMO), were carried out using Gaussian 09 software. NBO analysis evaluated the charge migration from one interacting molecule to another. However, the formation of a new energy level due to interaction of the two moieties (sensor and analyte) was explored through DOS and FMO analysis. Multiwfn and VMD software were used to analyze the type of non-covalent interactions (NCIs), such as electrostatic, van der Waals, and repulsive forces, between two interacting molecules (sensor and analyte). NCI analysis was performed to get a 2D reduced density gradient (RDG) plot and 3D isosurface of the sensor and analyte complex.

Results and discussion

Aggregation-induced emission enhancement (AIEE) features

The addition of water in to organic molecules leads to the formation of aggregates, which can eventually result in an alteration of the photophysical properties of organic molecules.[55] To evaluate the impact of water on the photophysical properties of the **ECX** sensor, 0–90% water was added into a 50 μM solution of the **ECX** sensor in DMF. The **ECX** sensor exhibited weak emission in pure DMF, but upon the addition of water the emission intensity of surprisingly increased along with a shift in the wavelength from almost 360 nm to 373 nm, which showed that the **ECX** sensor was AIEE active (Fig. 1a). This shift in the wavelength was due to the formation of "J type aggregates" resulting from the head to tail overlapping of the molecules. Bathochromic shifts do not always mean "J-aggregates" will form, but it may occur due to the solvent interaction. In the case of solvent interaction, the shift in the wavelength is comparatively smaller than the shift due to "J-aggregates",

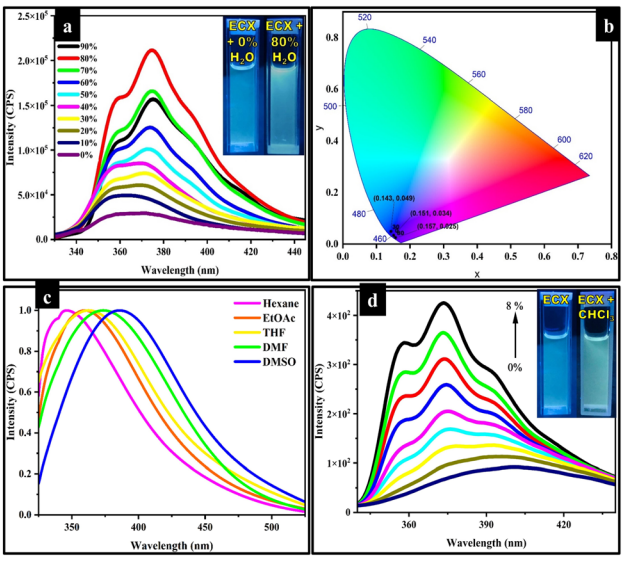

Fig. 1 (a) Emission spectra of the **ECX** sensor (50 μM) upon increasing f_w from 0 to 90% (b) CIE chromaticity diagram for the water fractions (c) emission spectra of the **ECX** sensor in various solvents and (d) fluorescence emission of the **ECX** sensor with increasing the chloroform percentage.

which was is typically less than 10 nm, though here a shift of about 13 nm was observed. Furthermore, in the case of solvent interaction, the shape of the peak usually remains broad and does not change with increasing the concentration of the solvent, but here the peak got sharper when increasing the percentage of water, which evidenced the formation of "J-aggregates".[56,57] The emission intensity of the **ECX** sensor increased linearly along with a slight red-shift in the emission wavelength upon the addition of up to 80% water, but then declined with further increasing this to a 90% water fraction (f_w). In the CIE chromaticity diagram, black dots could be seen in the purplish-blue region, showing the 0%, 30%, and 80% water fractions at (0.151, 0.034), (0.143, 0.049), and (0.157, 0.025), respectively (Fig. 1b). DLS analysis was also performed and demonstrated the particle size of the actual **ECX** sensor in pure DMF with 0% water and also with 80% water, which evidenced the formation of aggregates with the increasing water percentage. Specifically, the DLS results depicted that the size of the **ECX** sensor increased from 231.2 nm in 0% f_w to 290.4 nm in 80% f_w (Fig. S1†). The formation of aggregates in the presence of water tended to restrict the intramolecular rotations in the **ECX** sensor, which led to the opening of the radiative pathway and hence enhanced fluorescence emission intensity was observed. The three phenyl rings in the structure of the **ECX** sensor were connected through single bonds, and were rotatable in the pure DMF solution. However, rotation across these single bonds became restricted by the addition of water, consequently resulting in an enhancement of the emission intensity. Moreover, the structure of the **ECX** sensor became planarized with the formation of aggregates, which is the plausible reason for its enhanced emission. Specifically, the reduction in the emission intensity of the **ECX** sensor from 80 to 90% of f_w might be a result of π–π stacking of the **ECX** sensor's molecules.

Solvatochromism

To investigate the photophysical properties of the **ECX** sensor, emission studies were performed in various solvents with different polarities. The emission behavior of the freely rotatable phenyl rings in the **ECX** sensor was explored in different solvents. The ground state or excited state of a sensor can be affected by the nature of the solvent, which tends to shift the maximum emission wavelength of the sensor.[58,59] Various solvents, including hexane, tetrahydrofuran (THF), ethyl acetate (EtOAc), *N*,*N*-dimethylformamide (DMF), and dimethyl sulfoxide (DMSO). were chosen to study the emission behavior of the **ECX** sensor. For this purpose, a 50 μM solution of the **ECX** sensor was prepared in 1000 μL of each solvent. The emission spectra of the **ECX** sensor in all the selected solvents were obtained at 305 nm excitation wavelength. Interestingly, the maximum emission wavelength of the **ECX** sensor was shifted from 346 nm for hexane, 358 nm for ethyl acetate, 361 nm for THF, 373 nm for DMF, to 386 nm for DMSO. This red-shift of 40 nm in the emission maxima of the **ECX** sensor was due to the change in polarity of the solvents from non-polar to polar (Fig. 1c). The excited state of the **ECX** sensor's molecules possessing a greater dipole moment get stabilized by the interaction with solvents of varying polarity due to the dipoles of the solvent molecules. As a result, the energy gap is reduced and the emission spectrum is shifted to a longer wavelength, thereby showing a bathochromic shift. In other words, polar solvents stabilized the excited state of the **ECX** sensor, leading to a reduced gap between the ground state and excited state, which resulted in the emission of low energy photons at longer wavelength. Furthermore, the impact of solvent polarity on the fluorescence emission of the **ECX** sensor was investigated through Lippert–Mataga plots of the polarizability of the solvent (Δf) and the Stokes shift (Fig. S2†). A straight line in the Lippert–Mataga plots between the Stokes shift and Δf was obtained, which demonstrated the emissive behavior of the **ECX** sensor in different solvents. These results revealed that the **ECX** sensor can be employed to distinguish different solvents based on polarity. The **ECX** sensor demonstrated a substantial fluorescence emission and appropriate Stokes shift in DMF. Hence DMF was selected as a suitable solvent for the further studies.

Chloroform sensing

The **ECX** sensor was also utilized to determine the percentage of chloroform in DCM. In this perspective, a stock solution of the sensor **ECX** was made in 10 mL DCM. Then, 50 μM of this stock solution was titrated with 1–8% chloroform. The emission intensity of the **ECX** sensor increased when increasing the percentage of chloroform when it was radiated at the excitation wavelength of 285 nm. The increase in the emission intensity of the **ECX** sensor demonstrated that there might be a sort of interaction present between the chloroform and **ECX** through which the chloroform could be sensed. It was also observed that the emission wavelength of the **ECX** sensor was shifted to the blue region and a shoulder started appearing in the peaks with the rise in chloroform percentage (Fig. 1d). As chloroform is non-polar in nature compared to the DCM it destabilized the excited state of the sensor molecule, resulting in the increased energy gap and shift of the emission toward shorter wavelength, that is, blue-shift. As the emission spectrum of the **ECX** sensor showed a blue-shift, it verified there was an interaction of chloroform with the **ECX** sensor. Furthermore, the less stabilized excited electrons of the **ECX** sensor became de-excited through the radiative pathway, which consequently enhanced the emission intensity of the **ECX** sensor.[60] To determine to what extent **ECX** could detect the presence of chloroform in DCM, a 2D Benesi–Hildebrand graph was generated. The calculated value of LOD for chloroform was 0.2% v/v, as determined by the formula $3\sigma/S$ (Fig. S3†).

Selective sensing of F^-

To investigate the sensing capability of **ECX** for F^-, titration experiments were performed in a DMF : water (1 : 4, v/v) solution. Experiments were performed in the presence of different anions, including F^-, CH_3COO^-, HSO_4^-, CN^-, Cl^-, SO_4^{2-}, Br^-, I^-, ClO^-, and NO_3^-, varying concentrations from 0 to 50 μM and the **ECX** sensor (50 μM) in DMF : water (1 : 4, v/v). The emission intensity of the **ECX** sensor changed only when it was titrated against F^-, whereby a significant enhancement in the emission

intensity was noticed with increasing the concentration of F^-. The 3D Benesi–Hildebrand graph revealed that the **ECX** sensor was highly selective toward F^-, while all the other anions did not show any significant change in emission intensity for the **ECX** sensor (Fig. 2a).

Moreover, the binding efficiency of the sensor with F^- was investigated through the fluorescence titration experiments by varying the concentration of F^- from 0 to 50 μM, and it was found that the fluorescence emission spectrum demonstrated an enhancement in the fluorescence emission with highest intensity at 373 nm (Fig. 2b). To elucidate the sensitivity of the **ECX** sensor toward F^-, a 2D Benesi–Hildebrand plot was obtained of the relative emission intensity (I/I_o) of the **ECX** sensor and the concentration of F^- (Fig. 2c), which allowed determining the association constant (K_a) as 9.8×10^4, verifying the excellent sensitivity of the **ECX** sensor toward F^-. Furthermore, the limit of detection (LOD) of 20 nM was calculated from the Benesi–Hildebrand plot using the formula $3\sigma/S$, which was lower than that of the previously reported fluoride sensors (Table S1†). The calculated limit of quantification (LOQ) was 66.6 nM. Additionally, with the help of SEM analysis, the morphological structure of the **ECX**-F^- complex was also observed and appeared to be needle-like (Fig. 2d). Similarly, DLS analysis showed that the size of the **ECX** increased from 290.4 nm to 320.1 nm after interaction with F^- (Fig. S4†).

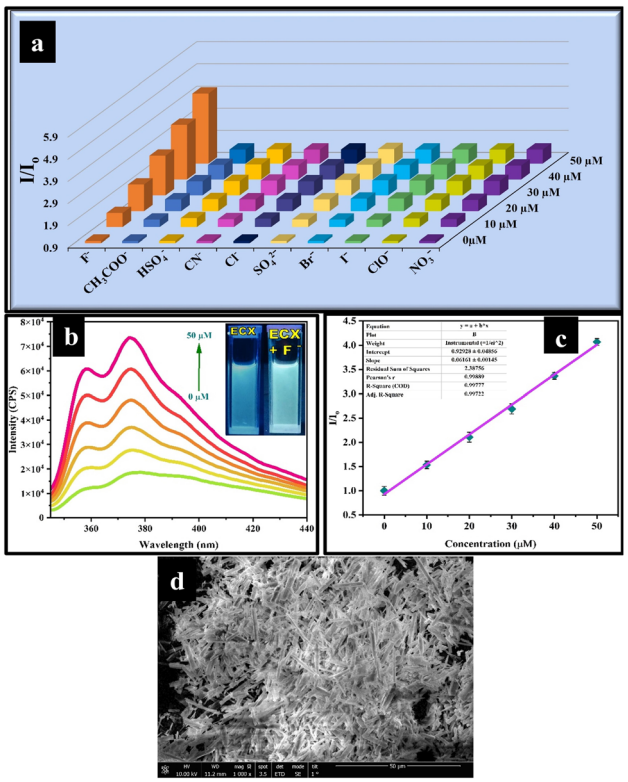

Fig. 2 (a) 3D Benesi–Hildebrand plot of the **ECX** sensor against various anions (b) emission spectra of the **ECX** sensor after successive additions of F^- (0–50 μM) (c) Benesi–Hildebrand plot of the **ECX** sensor against F^- and (d) SEM image of the **ECX**-F^- complex.

Plausible sensing mechanism

To explore the interaction in the **ECX**-F^- complex, NMR and fluorescence titration experiments were conducted. In the ^{1}H-NMR spectrum, the peaks at 8.32–8.33 ppm and 7.20 ppm were slightly shifted to 8.28–8.27 ppm and 7.19 ppm, respectively (Fig. 3a). Similarly, a slight change in the peaks was seen in the ^{13}C-NMR spectrum. The carbon peaks at 130.63, 136.00, 140.72, 149.86, and 152.75 were slightly shifted to 130.70, 135.99, 140.50, 149.69, and 152.63, respectively (Fig. 3b) which showed the existence of non-covalent interactions between **ECX** and F^-. LC-MS titration experiments were performed for the same reason and it was observed that other than the change in retention time from 1.09 to 1.11, no significant change was seen in the spectrum of **ECX** after the addition of 1 equivalent of F^-. In the subsequent solution containing **ECX** and F^- (1 : 1 equiv.), **ECX** took a slightly longer time in the column, which led to an increase in retention time (Fig. 3c). The maximum emission wavelength (λ_{max}) of the **ECX** sensor appeared at 373 nm. Fluorescence titration experiments of the **ECX** sensor demonstrated that the addition of F^- into the sensor neither induced any red- nor blue-shift in λ_{max} (Fig. 2b). The only noticeable change was the increment in the emission intensity of the **ECX** sensor, which revealed that the type of interaction between the sensor **ECX** and F^- was purely non-covalent. Moreover, it was inferred from the UV-Vis titration experiments that there was no red- or blue-shift in the maximum absorption wavelength of the **ECX** sensor after the additions of 10 μM and 30 μM fluoride, and only the intensity changed (Fig. S5†). The absorbance of the **ECX** sensor lay in the range of 240–300 nm. These emission and absorption titration experiments confirmed the presence of non-covalent interactions between the **ECX** sensor and F^-.

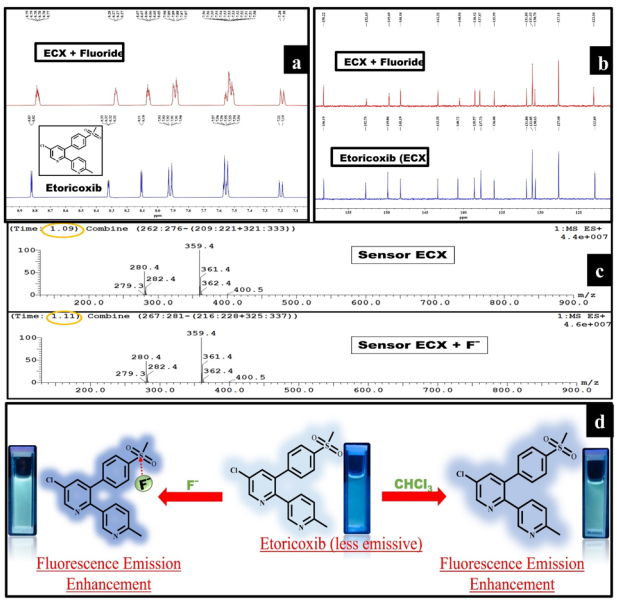

Fig. 3 (a) ^{1}H-NMR titration spectra, (b) ^{13}C-NMR titration spectra, and (c) LC-MS titration spectra of **ECX** and **ECX**-F^-. (d) Representative mechanism for etoricoxib (**ECX**) serving as a sensor for F^- ion and chloroform detection.

Furthermore, the continuous variance method was employed to explicate the binding stoichiometry of the **ECX** sensor and F^-. In this perspective, equimolar solutions of **ECX** and F^- were prepared. A Job's plot was developed of the relative emission intensity with varying the mole fraction of F^-. The emission intensity of the **ECX** sensor was analyzed by increasing the mole fractions of F^- from 0 to 1.0 equivalent, during which the overall concentration of 100 μM was kept constant. The highest relative emission intensity was obtained at a 0.5 mole fraction of F^-, which indicated the binding stoichiometry to be 1 : 1 (Fig. S6†). The Job's plot elucidated that one molecule of **ECX** interacted with a single F^- ion. The remarkable selectivity and excellent sensitivity of the **ECX** sensor toward F^- compelled us to explore its feasible detection mechanism to explain the cause of the enhanced fluorescence emission intensity of the **ECX** sensor upon interaction with F^-. **ECX** showed significant fluorescence emission due to electron delocalization throughout the system. Electronic charge resonated from the π electrons of two oxygen atoms to sulfur and between the phenyl ring system, which resulted in the **ECX** sensor's excellent emission. F^- is a strong nucleophile so it interacts with the sulfur as the electrophilic site in the **ECX** sensor, resulting in enhanced electronic delocalization due to which the fluorescence emission intensity increased. Furthermore, the small size of the F^- ion allowed it to easily penetrate the cavity of the **ECX** sensor and become attached to sulfur. The other electronegative ions, such as Cl^-, Br^-, and I^-, were not detected due to their large size. The interaction of F^- with the **ECX** sensor was electrostatic in nature, for which further evidence was provided through the DFT calculations. The 2D and 3D NCI analyses confirmed the presence of van der Waals interaction between the **ECX** sensor and F^-[61,62] (Fig. 3d).

Influence of interferences in fluoride sensing

It is important for a sensor to retain its selectivity and sensitivity toward the selected analyte in the presence of other competing analytes and in varying environmental conditions. Here, we studied the fluorescence emission of the **ECX** sensor for better understanding its sensing behavior toward fluoride ions in the presence of several available metal ions and neutral compounds (100 μM). These compounds included Al^{3+}, Ca^{2+}, Cu^{2+}, Fe^{2+}, Fe^{3+}, K^+, Li^+, Mg^{2+}, Na^+, Ni^{2+}, Zn^{2+}, H_2O_2, caffeic acid, citric acid, fructose, glucose, gallic acid, and glutamic acid. The experimental results suggested that the sensing behavior of the **ECX** sensor toward fluoride was the same in the presence and absence of interfering analytes (Fig. S7†). Moreover, the stability of the sensor was tested in a varying range of pH from pH 6–9 (Fig. S8†). The results showed that the **ECX** sensor could efficiently detect fluoride ions at different pH, suggesting the potential of sensor to be used for on-site applications under harsh conditions. For the same reason, the effect of temperature on the **ECX** sensing performance was tested. A solution of the **ECX** sensor (50 μM) was prepared in DMF : water (1 : 4, v/v) with 50 μM fluoride in it, and its emission intensity was recorded after heating it to 20–80 °C. The recorded emission results suggested that the detection of fluoride by the sensor was the same even at different temperatures (Fig. S9†). Furthermore, the photostability of a sensor is important for practical application. To test the photostability, a solution of 50 μM sensor and 50 μM fluoride was subjected to irradiation for different time periods. According to the obtained emission results, the **ECX** sensor showed good photostability and there was no change in its sensing ability for fluoride (Fig. S10†). After the photostability, the response time of a sensor is always a crucial parameter. Therefore, experiments were conducted with solutions of the **ECX** sensor and F^- to study the emission intensity at 20–80 s time intervals. Sensor **ECX** displayed an unchanged emission behavior with a very low response time (Fig. S11†).

Density functional theory studies

Thermodynamic stability and molecular orbital analysis. To illustrate the thermodynamic stabilities of the **ECX** sensor and F^-, the interaction energies at different possible sites were calculated. Geometry optimization was performed before calculating the interaction energies to get the lowest stable ground state. Specifically, the interaction energies were calculated at two different interaction sites I and II. The maximum interaction energy of **ECX** with F^- was at site I, which was calculated as -59.95 kJ mol^{-1} (Fig. S12†). The most stable interaction site was chosen based on the interaction energy values. Sites that exhibit the maximum value of interaction energy correspond to higher stability. The electronic properties of the **ECX** sensor and **ECX**-F^- complex were studied through FMO and DOS analysis. These electronic properties demonstrated the sensitivity of the **ECX** sensor toward F^-. The HOMO–LUMO energy values and HUMO–LUMO energy gap of the **ECX** sensor and **ECX**-F^- complex were also calculated. The reduction in the HOMO–LUMO gap demonstrated excellent sensitivity, while an increase in this gap indicated the resistance among the interacting moieties. The nucleophilic F^- ion interacted with the electrophilic site of the **ECX** sensor and the HOMO–LUMO energy band gap was reduced to 0.56 eV from 4.58 eV. Before the interaction, the HOMO–LUMO energy levels of the **ECX** sensor were at -6.46 and -1.82 eV, and were shifted to -0.71 and 1.25 eV after interaction with F^-. Furthermore, the DOS spectra clearly showed the HOMO–LUMO gap reduction, which indicated the sensor's excellent sensitivity toward F^- (Fig. 4a and b).

Reduce dentistry gradient and natural bond orbital aspects. For understanding the type of non-covalent interaction present between the **ECX** sensor and F^-, NCI analysis was performed. These non-covalent interactions involve van der Waals interactions, hydrogen bonding, and steric repulsive forces. To demonstrate such interactions between the **ECX** sensor and F^-, 2D and 3D NCI graphs were developed. The green dotted lines in the 2D RDG plot indicate the presence of van der Waals interaction between the sulfur of the **ECX** sensor and F^-, while the red dotted lines depict the repulsions between these two interacting species (Fig. 4c).

Likewise, the 3D isosurface of the **ECX**-F^- complex also showed a green patch between **ECX** and F^- which indicates the van der Waals interaction, while the red contour between the **ECX** and F^- represents the repulsion between these interacting

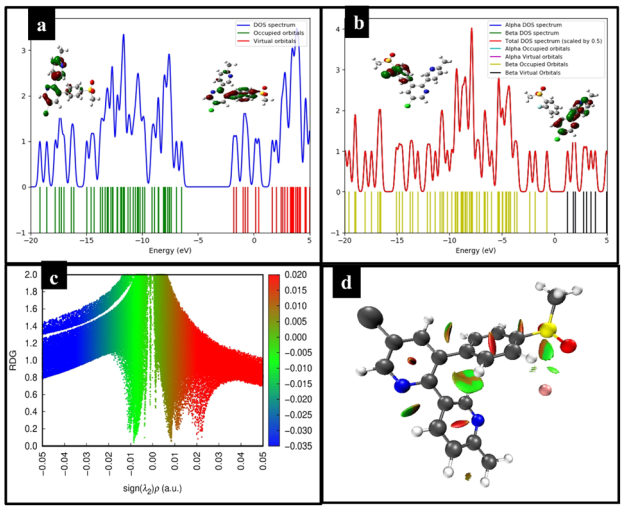

Fig. 4 (a) Frontier molecular orbital analysis (FMO) and density of states (DOS) spectra of the **ECX** sensor and (b) **ECX**-F^- complex (c) 2D RDG plot and (d) 3D isosurface of the non-covalent interactions (NCI) in the **ECX**-F^- complex.

species (Fig. 4d). To examine the transfer of electron density and hyper-conjugative interactions between the interacting species **ECX** and F^-, NBO analysis was carried out. To determine the charge transfer, NBO analysis was performed on ωB97XD/6-31G(d,p) functional. The observed charge transfer from F^- to **ECX** during the interaction was −0.1512 e^-.

Practical applications

Detection of moisture in raw building materials. Construction failure is often related to the presence of moisture in the raw building materials. Thus, having a sensor that can detect moisture in building materials is highly desired. For this reason, cement, sand, and fly ash samples (1 g) were collected from construction sites. These samples were soaked with dry DMF solvent, and after filtration, the moisture content was removed with the DMF, leaving behind dry raw materials. Furthermore, some samples were dried in an oven at 90 °C, which led to a 5% decrease in weight of the raw materials, confirming the presence of moisture before drying. Later, these samples were spiked with 2–10% water. The relative fluorescence emission was observed for the water-absorbed DMF, oven-dried, and water-spiked samples containing the **ECX** sensor (50 μM), and the spectra showed the highest percentage of water content was in the fly ash (Fig. S13†). With 97.1% recovery results in the fly ash samples, the **ECX** sensor demonstrated its potential as a suitable sensor for the detection of moisture in raw building materials (Table S2†).

Detection of fluoride in toothpaste and water samples. From the previously performed anti-interference experiments, a good response by the **ECX** sensor was seen toward fluoride ions, which led us to investigate the sensing potential of the **ECX** sensor in real samples. Considering the widespread use of fluoride in toothpaste, two types of toothpaste were selected, one that contains a high concentration of fluoride (Sensodyne 1450 ppm) as Sample A and another with a lower amount of fluoride (Colgate Max fresh 1100 ppm) As Sample B. First, 1000 mg of each toothpaste was added to a 100 mL water solution and subjected to centrifugation after being soaked for 12 h at room temperature, which led to the deposition of fluoride in the water. The obtained supernatant was filtered and 10–50 μL of each solution was added to a 50 μM solution of **ECX** in DMF : water (1 : 4, v/v). The prepared solutions were scanned to the study fluorescence emission. An enhanced fluorescence emission was noted in Sample A compared to Sample B, showing the presence of a higher quantity of fluoride in the sample (Fig. S14a†). With 98% recovery, the probe could efficiently detect fluoride in toothpaste (Table S2†). Moreover, experiments were performed to investigate the detection of fluoride in water samples. For this purpose, water samples were spiked with 0 μM to 50 μM fluoride and the fluorescence emission spectra were recorded for the water samples with the spiked concentration of the **ECX** sensor (50 μM). Enhanced emission was seen in the case of the fluoride-spiked samples, demonstrating the efficient detection of fluoride by the **ECX** sensor (Fig. S14b†), showing that it is suitable for use as a fluoride sensor for real samples.

Conclusion

Etoricoxib (**ECX**), having heteroatoms and π-conjugation, exhibited remarkable photophysical properties as studied through fluorescence and UV-Vis spectroscopy. **ECX** showed a maximum fluorescence emission at 373 nm wavelength for the fluorescence spectra recorded with increasing water fractions. The emission intensity was enhanced significantly with increasing water fractions, which was a result of the aggregation-induced emission enhancement (AIEE) characteristic of **ECX**. An emission enhancement was seen with up to 80% water; however, notable quenching was observed with 90% water, which might be a result of π–π stacking. **ECX** was optimized in DMF : water (1 : 4, v/v) for all the experiments. Considering the structure and photophysical properties of **ECX**, it was studied as a sensor for analytes, and it successfully detected fluoride ions with a 20 nM limit of detection. Furthermore, chloroform was further detected by **ECX** down to 0.2% v/v. When **ECX** was titrated against several competing analytes, no noticeable change was seen for any analyte and a significant enhancement in emission intensity of the sensor was seen only for fluoride which showed that the sensor was highly selective and sensitive toward fluoride, as further supported through the SEM and DLS analyses. Also, this sensing of fluoride remained unaffected in the presence of possible interfering species, as investigated through fluorescence titration experiments, indicating the high selectivity and sensitivity of the **ECX** sensor. Also, the sensor remained stable within a pH range of 6–9 and different temperatures from 20 to 80 °C, which had no prominent effect on its sensing potential for fluoride. When the emission of the sensor with fluoride was studied after exposure to high energy radiation, the sensor exhibited high stability, indicating that it was free from the photobleaching effect. Moreover, through studies of the behavior of the sensor

against fluoride at different time intervals from 20 to 80 seconds, it was concluded that the activity of the sensor was not dependent on time. DFT provided further evidence for the existence of non-covalent interactions between the **ECX** sensor and fluoride. Thermodynamic stability studies showed -59.95 kJ mol^{-1} interaction energy at site I of the sensor and fluoride. Through frontier molecular orbital (FMO) analysis along with density of state (DOS) analysis, a reduction of the HOMO–LUMO energy gap was seen from 4.58 eV to 0.56 eV. Furthermore, the presence of van der Waals forces was further confirmed through non-covalent interaction (NCI) analysis and a charge transfer of -0.1512 e$^-$ from the fluoride to sensor was calculated through natural bond orbital (NBO) analysis.

Data availability

The data supporting this article have been included as part of the ESI.†

Author contributions

Sohail Anjum Shahzad: supervision, conceptualization, methodology, visualization, validation, investigation, project administration, funding acquisition, writing-review & editing. **Tayyeba Javid**: visualization, methodology, software, formal analysis, investigation, writing-original draft. **Mohammed A. Assiri**: methodology, funding acquisition. **Aqsa Pervaiz**: methodology, investigation, formal analysis. **Hasher Irshad**: investigation, conceptualization, methodology, validation. **Fu-She Han**: methodology, visualization, validation. **Di Demi He**: methodology, visualization, validation.

Conflicts of interest

The authors declare that they have no known competing financial interests or personal relationships that could have appeared to influence the work reported in this paper.

Acknowledgements

The authors extend their appreciation to University Higher Education Fund for funding this research work under Research Support Program for Central labs at King Khalid University through the project number CL/PRI/C/16.

Notes and references

1 A. Brzechwa-Chodzyńska, W. Drożdż, J. Harrowfield and A. R. Stefankiewicz, *Coord. Chem. Rev.*, 2021, **434**, 213820.
2 B. R. Jali, A. K. Barick, P. Mohapatra and S. K. Sahoo, *J. Fluorene Chem.*, 2021, **244**, 109744.
3 A. W. Czarnik, Fluorescent chemosensors for ion and molecule recognition, in *ACS Symposium Series*, ACS Press, 1993, p. 538.
4 K. C. Yan, A. Steinbrueck, A. C. Sedgwick and T. D. James, *Front. Sens.*, 2021, **2**, 731928.
5 D. Wu, A. C. Sedgwick, T. Gunnlaugsson, E. U. Akkaya, J. Yoon and T. D. James, *Chem. Soc. Rev.*, 2017, **46**, 7105–7123.
6 N. Dey and S. Bhattacharya, *Chem.–Asian J.*, 2020, **15**, 1759–1779.
7 G. Boivin, M. C. Chapuy, C. A. Baud and P. J. Meunier, *J. Bone Miner. Res.*, 2020, **3**, 497–502.
8 B. A. Menke, C. Ryu, G. A. Justin, R. V. Chundury, B. Hayek, M. R. Debiec and S. Yeh, *Front. Toxicol.*, 2023, **5**, 1281041.
9 H. Kabir, A. K. Gupta and S. Tripathy, *Crit. Rev. Environ. Sci. Technol.*, 2020, **50**, 1116–1193.
10 A. Dey Bhowmik, P. Shaw, P. Mondal, A. Chakraborty, M. Sudarshan and A. Chattopadhyay, *Biol. Trace Elem. Res.*, 2021, **199**, 3035–3044.
11 H. Ottappilakkil, S. Babu, S. Balasubramanian, S. Manoharan and E. Perumal, *Biol. Trace Elem. Res.*, 2023, **201**, 1214–1236.
12 G. A. Castiblanco-Rubio and E. A. Martinez-Mier, *Metabolites*, 2022, **12**, 324.
13 N. R. Johnston and S. A. Strobel, *Arch. Toxicol.*, 2020, **94**, 1051–1069.
14 J. Lavalle-Carrasco, N. Molina-Frechero, M. Nevárez-Rascón, L. Sánchez-Pérez, A. Hamdan-Partida, R. González-González, D. Cassi, M. A. Isiordia-Espinoza and R. Bologna-Molina, *Int. J. Environ. Res. Public Health*, 2021, **18**, 317.
15 D. Udhayakumari, *Spectrochim. Acta, Part A*, 2020, **228**, 117817.
16 A. K. Tolkou, N. Manousi, G. A. Zachariadis, I. A. Katsoyiannis and E. A. Deliyanni, *Sustainability*, 2021, **13**, 7061.
17 S. Majeed, T. A. Khan, M. T. Waseem, H. M. Junaid, A. M. Khan and S. A. Shahzad, *J. Photochem. Photobiol., A*, 2022, **431**, 114062.
18 R. Hu, A. Qin and B. Z. Tang, *Prog. Polym. Sci.*, 2020, **100**, 101176.
19 F. Würthner, *Angew. Chem., Int. Ed.*, 2020, **59**, 14192–14196.
20 M. A. Assiri, S. Hanif, H. M. Junaid, A. Hamad, H. Irshad, M. Yar, W. Rauf and S. A. Shahzad, *J. Photochem. Photobiol., A*, 2023, **438**, 114514.
21 Y. Lin, A. Yu, J. Wang, D. Kong, H. Liu, J. Li and C. Jia, *RSC Adv.*, 2022, **12**, 16772–16778.
22 J. Qi, X. Hu, X. Dong, Y. Lu, H. Lu, W. Zhao and W. Wu, *Adv. Drug Delivery Rev.*, 2019, **143**, 206–225.
23 S. Hussain, X. Chen, Y. Gao, H. Song, X. Tian, Y. He, A. Abbas, M. A. Afroz, Y. Hao and R. Gao, *Adv. Opt. Mater.*, 2023, 2202851.
24 M. Kang, Z. Zhang, N. Song, M. Li, P. Sun, X. Chen, D. Wang and B. Z. Tang, *Aggregate*, 2020, **1**, 80–106.
25 S. Liu, G. Feng, B. Z. Tang and B. Liu, *Chem. Sci.*, 2021, **12**, 6488–6506.
26 K. Zhang, J. Shu, W. Chu, X. Liu, B. Xu and W. Jiang, *Dyes Pigm.*, 2021, **185**, 108898.
27 İ. Sıdır, T. Sarı, Y. G. Sıdır and H. Berber, *J. Mol. Liq.*, 2022, **346**, 117075.
28 M. A. Assiri, H. M. Junaid, M. T. Waseem, A. Hamad, S. H. Shah, J. Iqbal, W. Rauf and S. A. Shahzad, *Anal. Chim. Acta*, 2022, **1234**, 340516.

29 X. Dong, W. Wan, L. Zeng, W. Jin, Y. Huang, D. Shen, Y. Bai, Q. Zhao, L. Zhang and Y. Liu, *Anal. Chem.*, 2021, **93**, 16447–16455.
30 T. Javid, S. A. Shahzad, M. A. Assiri, A. Pervaiz, Khadija and H. Irshad, *Microchem. J.*, 2024, 109934.
31 S. Rafique, A. Y. A. Alzahrani, Khadija, H. Irshad, A. M. Khan and S. A. Shahzad, *Spectrochim. Acta, Part A*, 2023, 122946.
32 M. A. Assiri, F. Munir, M. T. Waseem, H. Irshad, W. Rauf and S. A. Shahzad, *Microchem. J.*, 2023, **193**, 109220.
33 K. O. Khan, M. A. Assiri, H. Irshad, S. Rafique, A. M. Khan, A. K. Khan, M. Imran and S. A. Shahzad, *J. Photochem. Photobiol., A*, 2023, **442**, 114805.
34 H. Irshad, M. A. Assiri, Khadija, S. Rafique, A. M. Khan, M. Imran and S. A. Shahzad, *Spectrochim. Acta, Part A*, 2023, **300**, 122934.
35 T. Javid, M. A. Assiri, A. Pervaiz, H. Irshad, K. Qvortrup and S. A. Shahzad, *J. Mol. Liq.*, 2024, **409**, 125526.
36 S. Hussain, H. M. Junaid, M. T. Waseem, W. Rauf, A. J. Shaikh and S. A. Shahzad, *Spectrochim. Acta, Part A*, 2022, **272**, 121021.
37 Khadija, H. Irshad, S. Rafique, A. M. Khan, S. Nawazish, H. ur Rehman, M. Imran, S. A. Shahzad and U. Farooq, *Spectrochim. Acta, Part A*, 2023, **290**, 122273.
38 A. Pervaiz, S. A. Shahzad, M. A. Assiri, T. Javid, H. Irshad and K. O. Khan, *Spectrochim. Acta, Part A*, 2024, **313**, 124121.
39 S. Rafique, H. Irshad, S. Majeed, Khadija, R. Rubab, M. Imran, A. M. Khan and S. A. Shahzad, *J. Photochem. Photobiol., A*, 2023, **437**, 114459.
40 M. Z. Ullah, S. A. Shahzad, M. A. Assiri, H. Irshad, S. Rafique, S. A. Shakir and A. Mumtaz, *Spectrochim. Acta, Part A*, 2024, **306**, 123607.
41 H. Rabale, H. Irshad, A. Pervaiz, S. S. Almujri, A. Y. A. Alzahrani, M. Z. Ullah and S. A. Shahzad, *Microchem. J.*, 2024, **205**, 111312.
42 H. H. Fang, J. Hsu and J. G. J. Su, *Toxicology*, 2023, **499**, 153658.
43 A. Majeed, M. A. Assiri, H. Irshad, Khadija, M. Z. Ullah and S. A. Shahzad, *Microchem. J.*, 2024, 110640.
44 I. Ullah, S. A. Shahzad, M. A. Assiri, M. Z. Ullah, H. Irshad and U. Farooq, *Spectrochim. Acta, Part A*, 2024, 124224.
45 Sania, M. A. Assiri, S. Rafique, H. Irshad, Z. A. Khan, F. A. Khan and S. A. Shahzad, *J. Mol. Struct.*, 2024, **1307**, 137963.
46 A. Y. A. Alzahrani, K. O. Khan, S. Rafique, H. Irshad, Khadija, A. M. Khan and S. A. Shahzad, *Spectrochim. Acta, Part A*, 2023, **297**, 122745.
47 R. Khalid, S. A. Shahzad, M. A. Assiri, T. Javid, H. Irshad and M. Z. Ullah, *Microchem. J.*, 2024, **200**, 110264.
48 K. Khurshid, S. A. Shahzad, M. A. Assiri, A. Shabbir, T. Javid and H. Irshad, *RSC Adv.*, 2024, **14**, 21682–21691.
49 M. J. Frisch, G. W. Trucks, H. B. Schlegel, G. E. Scuseria, M. A. Robb, J. R. Cheeseman, G. Scalmani, V. Barone, B. Mennucci, G. A. Petersson, H. Nakatsuji, M. Caricato, X. Li, H. P. Hratchian, A. F. Izmaylov, J. Bloino, G. Zheng, J. L. Sonnenberg, M. Hada, M. Ehara, K. Toyota, R. Fukuda, J. Hasegawa, M. Ishida, T. Nakajima, Y. Honda, O. Kitao, H. Nakai, T. Vreven, J. A. Montgomery Jr, J. E. Peralta, F. Ogliaro, M. Bearpark, J. J. Heyd, E. Brothers, K. N. Kudin, V. N. Staroverov, T. Keith, R. Kobayashi, J. Normand, K. Raghavachari, A. Rendell, J. C. Burant, S. S. Iyengar, J. Tomasi, M. Cossi, N. Rega, J. M. Millam, M. Klene, J. E. Knox, J. B. Cross, V. Bakken, C. Adamo, J. Jaramillo, R. Gomperts, R. E. Stratmann, O. Yazyev, A. J. Austin, R. Cammi, C. Pomelli, J. W. Ochterski, R. L. Martin, K. Morokuma,V. G. Zakrzewski, G. A. Voth, P. Salvador, J. J. Dannenberg, S. Dapprich, A. D. Daniels, O. Farkas, J. B. Foresman, J. V. Ortiz, J. Cioslowski and D. J. Fox, *Gaussian 09, Revision D.01*, Gaussian, Inc., Wallingford CT, 2013.
50 N. M. O'boyle, A. L. Tenderholt and K. M. Langner, *J. Comput. Chem.*, 2008, **29**, 839–845.
51 T. Lu and F. Chen, *J. Comput. Chem.*, 2012, **33**, 580–592.
52 W. Humphrey, A. Dalke and K. Schulten, *J. Mol. Graphics*, 1996, **14**, 33–38.
53 C. Lee, W. Yang and R. G. Parr, *Phys. Rev. B:Condens. Matter Mater. Phys.*, 1988, **37**, 785.
54 J. D. Chai and M. Head-Gordon, *Phys. Chem. Chem. Phys.*, 2008, **10**, 6615–6620.
55 X. Zhang, Z. Chi, J. Zhang, H. Li, B. Xu, X. Li, S. Liu, Y. Zhang and J. Xu, *J. Phys. Chem. B*, 2011, **115**, 7606–7611.
56 A. Koti, J. Taneja and N. Periasamy, *Chem. Phys. Lett.*, 2003, **375**, 171–176.
57 P. W. Bohn, *Annu. Rev. Phys. Chem.*, 1993, **44**, 37–60.
58 M. Haidekker, T. Brady, D. Lichlyter and E. Theodorakis, *Bioorg. Chem.*, 2005, **33**, 415–425.
59 H. Irshad and K. Qvortrup, *J. Mol. Liq.*, 2024, 126049.
60 S. Patil, M. Wari, C. Y. Panicker and S. Inamdar, *Spectrochim. Acta, Part A*, 2014, **123**, 117–126.
61 T. Kharandiuk, E. J. Hussien, J. Cameron, R. Petrina, N. J. Findlay, R. Naumov, W. T. Klooster, S. J. Coles, Q. Ai and S. Goodlett, *Chem. Mater.*, 2019, **31**, 7070–7079.
62 M. Saito, T. Fukuhara, S. Kamimura, H. Ichikawa, H. Yoshida, T. Koganezawa, Y. Ie, Y. Tamai, H. D. Kim and H. Ohkita, *Adv. Energy Mater.*, 2020, **10**, 1903278.